

Self-calibration of LHAASO-KM2A electromagnetic particle detectors using single particles within extensive air showers

F. Aharonian,^{4,5} Q. An,^{6,7} Axikegu,⁸ L. X. Bai,⁹ Y. X. Bai,^{1,3} Y. W. Bao,¹⁰ D. Bastieri,¹¹ X. J. Bi,^{1,2,3} Y. J. Bi,^{1,3} J. T. Cai,¹¹ Z. Cao,^{1,2,3} Z. Cao,^{6,7} J. Chang,¹² J. F. Chang,^{1,3,6} E. S. Chen,^{1,2,3} L. Chen,^{1,2,3} L. Chen,¹³ L. Chen,⁸ M. J. Chen,^{1,3} M. L. Chen,^{1,3,6} Q. H. Chen,⁸ S. H. Chen,^{1,2,3} S. Z. Chen,^{1,3} T. L. Chen,¹⁴ Y. Chen,¹⁰ H. L. Cheng,^{2,14,15} N. Cheng,^{1,3} Y. D. Cheng,^{1,3} S. W. Cui,¹⁶ X. H. Cui,¹⁵ Y. D. Cui,¹⁷ B. D’Ettorre Piazzoli,¹⁸ B. Z. Dai,¹⁹ H. L. Dai,^{1,3,6} Z. G. Dai,⁷ Danzengluobu,¹⁴ D. della Volpe,²⁰ K. K. Duan,¹² J. H. Fan,¹¹ Y. Z. Fan,¹² Z. X. Fan,^{1,3} J. Fang,¹⁹ K. Fang,^{1,3} C. F. Feng,²¹ L. Feng,¹² S. H. Feng,^{1,3} X. T. Feng,²¹ Y. L. Feng,¹⁴ B. Gao,^{1,3} C. D. Gao,²¹ L. Q. Gao,^{1,2,3} Q. Gao,¹⁴ W. Gao,^{1,3} W. K. Gao,^{1,2,3} M. M. Ge,¹⁹ L. S. Geng,^{1,3} G. H. Gong,²² Q. B. Gou,^{1,3} M. H. Gu,^{1,3,6} F. L. Guo,¹³ J. G. Guo,^{1,2,3} X. L. Guo,⁸ Y. Q. Guo,^{1,3} Y. Y. Guo,¹² Y. A. Han,²³ H. H. He,^{1,2,3} H. N. He,¹² S. L. He,¹¹ X. B. He,¹⁷ Y. He,⁸ M. Heller,²⁰ Y. K. Hor,¹⁷ C. Hou,^{1,3} X. Hou,²⁴ H. B. Hu,^{1,2,3} Q. Hu,^{7,12} S. Hu,⁹ S. C. Hu,^{1,2,3} X. J. Hu,²² D. H. Huang,⁸ W. H. Huang,²¹ X. T. Huang,²¹ X. Y. Huang,¹² Y. Huang,^{1,2,3} Z. C. Huang,⁸ X. L. Ji,^{1,3,6} H. Y. Jia,⁸ K. Jia,²¹ K. Jiang,^{6,7} Z. J. Jiang,¹⁹ M. Jin,^{1,3} M. M. Kang,⁹ T. Ke,^{1,3} D. Kuleshov,²⁵ K. Levochkin,²⁵ B. B. Li,¹⁶ C. Li,^{6,7} C. Li,^{1,3} F. Li,^{1,3,6} H. B. Li,^{1,3} H. C. Li,^{1,3} H. Y. Li,^{7,12} J. Li,^{7,12} J. Li,⁷ J. Li,^{1,3,6} K. Li,^{1,3} W. L. Li,²¹ X. R. Li,^{1,3} X. Li,^{6,7} X. Li,⁸ Y. Z. Li,^{1,2,3} Z. Li,^{1,3} Z. Li,²⁶ E. W. Liang,²⁷ Y. F. Liang,²⁷ S. J. Lin,¹⁷ B. Liu,⁷ C. Liu,^{1,3} D. Liu,²¹ H. Liu,⁸ H. D. Liu,²³ J. Liu,^{1,3} J. L. Liu,²⁸ J. S. Liu,¹⁷ J. Y. Liu,^{1,3} M. Y. Liu,¹⁴ R. Y. Liu,¹⁰ S. M. Liu,⁸ W. Liu,^{1,3} Y. Liu,¹¹ Y. N. Liu,²² W. J. Long,⁸ R. Lu,¹⁹ Q. Luo,¹⁶ H. K. Lv,^{1,3,*} B. Q. Ma,²⁶ L. L. Ma,^{1,3} X. H. Ma,^{1,3} J. R. Mao,²⁴ A. Masood,⁸ Z. Min,^{1,3} W. Mitthumsiri,²⁹ Y. C. Nan,²¹ Z. W. Ou,¹⁷ B. Y. Pang,^{8,†} P. Pattarakijwanich,²⁹ Z. Y. Pei,¹¹ M. Y. Qi,^{1,3} Y. Q. Qi,¹⁶ B. Q. Qiao,^{1,3} J. J. Qin,⁷ D. Ruffolo,²⁹ A. Sáiz,²⁹ C. Y. Shao,¹⁷ L. Shao,¹⁶ O. Shchegolev,^{25,30} X. D. Sheng,^{1,3} J. Y. Shi,^{1,3} H. C. Song,²⁶ Yu. V. Stenkin,^{25,30} V. Stepanov,²⁵ Y. Su,¹² Q. N. Sun,⁸ X. N. Sun,²⁷ Z. B. Sun,³¹ P. H. T. Tam,¹⁷ Z. B. Tang,^{6,7} W. W. Tian,^{2,15} B. D. Wang,^{1,3} C. Wang,³¹ H. Wang,⁸ H. G. Wang,¹¹ J. C. Wang,²⁴ J. S. Wang,²⁸ L. P. Wang,²¹ L. Y. Wang,^{1,3} R. Wang,²¹ R. N. Wang,⁸ W. Wang,¹⁷ X. G. Wang,²⁷ X. Y. Wang,¹⁰ Y. Wang,⁸ Y. D. Wang,^{1,3} Y. J. Wang,^{1,3} Y. P. Wang,^{1,2,3} Z. H. Wang,⁹ Z. X. Wang,¹⁹ Z. Wang,²⁸ Z. Wang,^{1,3,6} D. M. Wei,¹² J. J. Wei,¹² Y. J. Wei,^{1,2,3} T. Wen,¹⁹ C. Y. Wu,^{1,3} H. R. Wu,^{1,3} S. Wu,^{1,3} X. F. Wu,¹² Y. S. Wu,⁷ S. Q. Xi,^{1,3} J. Xia,^{7,12} J. J. Xia,⁸ G. M. Xiang,^{2,13} D. X. Xiao,¹⁴ G. Xiao,^{1,3} G. G. Xin,^{1,3} Y. L. Xin,⁸ Y. Xing,¹³ Z. Xiong,^{1,2,3} D. L. Xu,²⁸ R. X. Xu,²⁶ L. Xue,²¹ D. H. Yan,²⁴ J. Z. Yan,¹² C. W. Yang,⁹ F. F. Yang,^{1,3,6} H. W. Yang,¹⁷ J. Y. Yang,¹⁷ L. L. Yang,¹⁷ M. J. Yang,^{1,3} R. Z. Yang,⁷ S. B. Yang,¹⁹ Y. H. Yao,⁹ Z. G. Yao,^{1,3} Y. M. Ye,²² L. Q. Yin,^{1,3} N. Yin,²¹ X. H. You,^{1,3} Z. Y. You,^{1,2,3} Y. H. Yu,⁷ Q. Yuan,¹² H. Yue,^{1,2,3} H. D. Zeng,¹² T. X. Zeng,^{1,3,6} W. Zeng,¹⁹ Z. K. Zeng,^{1,2,3} M. Zha,^{1,3} X. X. Zhai,^{1,3} B. B. Zhang,¹⁰ F. Zhang,⁸ H. M. Zhang,¹⁰ H. Y. Zhang,^{1,3} J. L. Zhang,¹⁵ L. X. Zhang,¹¹ L. Zhang,¹⁹ L. Zhang,¹⁶ P. F. Zhang,¹⁹ P. P. Zhang,^{7,12} R. Zhang,^{7,12} S. B. Zhang,^{2,15} S. R. Zhang,¹⁶ S. S. Zhang,^{1,3} X. Zhang,¹⁰ X. P. Zhang,^{1,3} Y. F. Zhang,⁸ Y. L. Zhang,^{1,3} Y. Zhang,^{1,12} Y. Zhang,^{1,3} B. Zhao,⁸ J. Zhao,^{1,3} L. Zhao,^{6,7} L. Z. Zhao,¹⁶ S. P. Zhao,^{12,21} F. Zheng,³¹ Y. Zheng,⁸ B. Zhou,^{1,3} H. Zhou,²⁸ J. N. Zhou,¹³ P. Zhou,¹⁰ R. Zhou,⁹ X. X. Zhou,⁸ C. G. Zhu,²¹ F. R. Zhu,⁸ H. Zhu,¹⁵ K. J. Zhu,^{1,2,3,6} and X. Zuo^{1,3}

(LHAASO Collaboration)

¹Key Laboratory of Particle Astrophysics & Experimental Physics Division & Computing Center, Institute of High Energy Physics, Chinese Academy of Sciences, 100049 Beijing, China

²University of Chinese Academy of Sciences, 100049 Beijing, China

³TIANFU Cosmic Ray Research Center, 610299 Chengdu, Sichuan, China

⁴Dublin Institute for Advanced Studies, 31 Fitzwilliam Place, 2 Dublin, Ireland

⁵Max-Planck-Institut für Nuclear Physics, P.O. Box 103980, 69029 Heidelberg, Germany

⁶State Key Laboratory of Particle Detection and Electronics, China

⁷University of Science and Technology of China, 230026 Hefei, Anhui, China

⁸School of Physical Science and Technology & School of Information Science and Technology, Southwest Jiaotong University, 610031 Chengdu, Sichuan, China

⁹College of Physics, Sichuan University, 610065 Chengdu, Sichuan, China

¹⁰School of Astronomy and Space Science, Nanjing University, 210023 Nanjing, Jiangsu, China

¹¹Center for Astrophysics, Guangzhou University, 510006 Guangzhou, Guangdong, China

¹²Key Laboratory of Dark Matter and Space Astronomy & Key Laboratory of Radio Astronomy, Purple Mountain Observatory, Chinese Academy of Sciences, 210023 Nanjing, Jiangsu, China

¹³Key Laboratory for Research in Galaxies and Cosmology, Shanghai Astronomical Observatory, Chinese Academy of Sciences, 200030 Shanghai, China

¹⁴Key Laboratory of Cosmic Rays (Tibet University), Ministry of Education, 850000 Lhasa, Tibet, China

- ¹⁵*National Astronomical Observatories, Chinese Academy of Sciences, 100101 Beijing, China*
¹⁶*Hebei Normal University, 050024 Shijiazhuang, Hebei, China*
¹⁷*School of Physics and Astronomy (Zhuhai) & School of Physics (Guangzhou) & Sino-French Institute of Nuclear Engineering and Technology (Zhuhai), Sun Yat-sen University, 519000 Zhuhai & 510275 Guangzhou, Guangdong, China*
¹⁸*Dipartimento di Fisica dell'Università di Napoli "Federico II", Complesso Universitario di Monte Sant'Angelo, via Cinthia, 80126 Napoli, Italy*
¹⁹*School of Physics and Astronomy, Yunnan University, 650091 Kunming, Yunnan, China*
²⁰*Département de Physique Nucléaire et Corpusculaire, Faculté de Sciences, Université de Genève, 24 Quai Ernest Ansermet, 1211 Geneva, Switzerland*
²¹*Institute of Frontier and Interdisciplinary Science, Shandong University, 266237 Qingdao, Shandong, China*
²²*Department of Engineering Physics, Tsinghua University, 100084 Beijing, China*
²³*School of Physics and Microelectronics, Zhengzhou University, 450001 Zhengzhou, Henan, China*
²⁴*Yunnan Observatories, Chinese Academy of Sciences, 650216 Kunming, Yunnan, China*
²⁵*Institute for Nuclear Research of Russian Academy of Sciences, 117312 Moscow, Russia*
²⁶*School of Physics, Peking University, 100871 Beijing, China*
²⁷*School of Physical Science and Technology, Guangxi University, 530004 Nanning, Guangxi, China*
²⁸*Tsung-Dao Lee Institute & School of Physics and Astronomy, Shanghai Jiao Tong University, 200240 Shanghai, China*
²⁹*Department of Physics, Faculty of Science, Mahidol University, 10400 Bangkok, Thailand*
³⁰*Moscow Institute of Physics and Technology, 141700 Moscow, Russia*
³¹*National Space Science Center, Chinese Academy of Sciences, 100190 Beijing, China*



(Received 15 April 2022; accepted 21 November 2022; published 22 December 2022)

In the Large High Altitude Air Shower Observatory (LHAASO), the square kilometer array, with 5249 electromagnetic particle detectors (EDs) and 1188 muon detectors, is deployed to explore the gamma-ray sources above 30 TeV with unprecedented sensitivity and to measure primary cosmic rays in the energy range from 10 TeV to 100 PeV. The energetic particles produced by extensive air showers can serve as a continuously available source for calibration of the numerous EDs over a large area. In this study, the detector untriggered probability is first proposed to estimate the particle density at different distances from the shower core and distinguish the characteristic single-particle signal detected by each ED. This method uses science data directly, and does not require prior knowledge of the cosmic-ray elemental composition or hadronic interaction model. Experimental results show that this self-calibration can be used to determine the number of particles detected by each ED with an accuracy better than 2% within a time scale of hours, which is adequate to meet the physics requirements of the LHAASO experiment. With this high efficiency and accuracy, this calibration also provides an ideal method to monitor the detector performance throughout an expected lifetime of > 10 years.

DOI: [10.1103/PhysRevD.106.122004](https://doi.org/10.1103/PhysRevD.106.122004)

I. INTRODUCTION

The Large High Altitude Air Shower Observatory (LHAASO) at Haizi Mountain (4410 m above sea level) in China has been operated with its full scale detector array since July 2021. It consists of three interconnected detector arrays, i.e., the square kilometer array (KM2A), with 5249 electromagnetic particle detectors (EDs) and 1188 muon detectors (MDs) deployed on a triangle grid with 15 and 30 m spacing, respectively, the 78 000 m² water Cherenkov

detector array (WCDA), and the wide field-of-view Cherenkov telescope array (WFCTA) with 18 telescopes, as illustrated in Fig. 1.

KM2A aims to explore high-energy gamma-ray sources above 30 TeV with unprecedented sensitivity and to measure primary cosmic rays in the energy range from 10 TeV to 100 PeV [1–6]. The energy reconstruction depends on the effective number of shower particles detected by each ED unit, for which a well-defined calibration approach, as an integral part of the ED design, is paramount. Since the uncertainties caused by the shower fluctuation at the observation location and the incomplete knowledge of the atmospheric conditions cannot be significantly reduced to less than 10% with reasonable efforts, the photomultiplier tube (PMT) output charge recorded by

* Corresponding author.
lvhk@ihep.ac.cn

† Corresponding author.
pangby@ihep.ac.cn

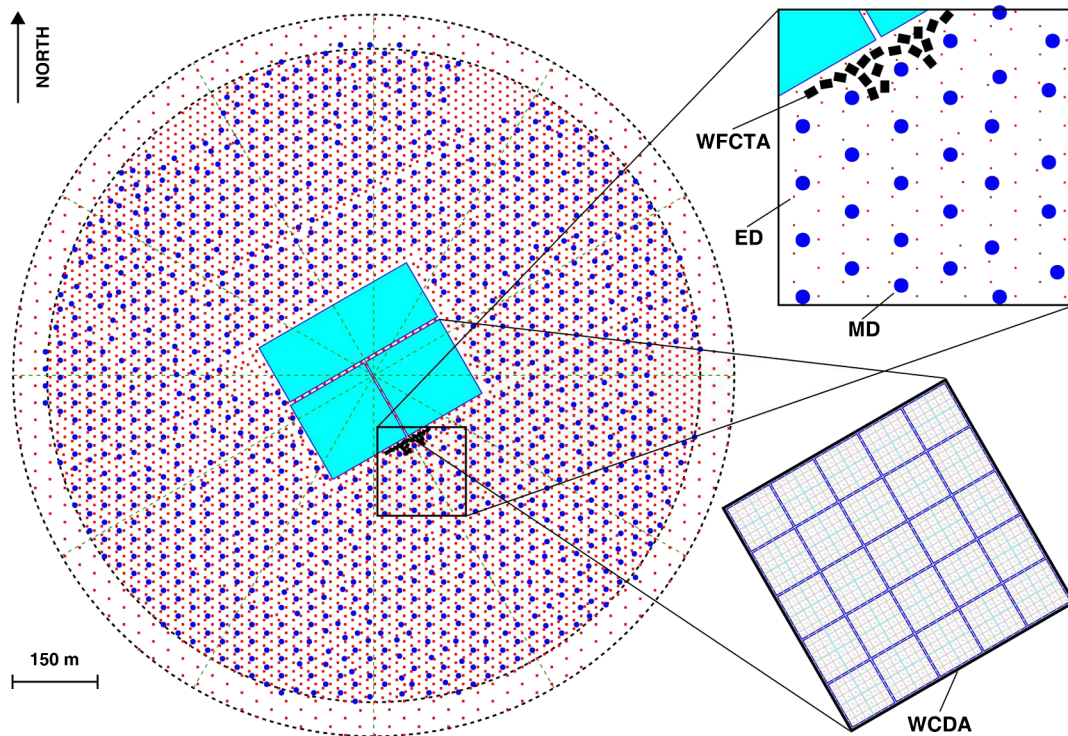


FIG. 1. Layout of the LHAASO experiment. It covers a total area of approximately 1.3 km^2 . Within 575 m of the center of KM2A, the EDs are deployed on a 15 m grid. Within the outskirts region, the ED spacing is enlarged to 30 m. The skirt array is used to identify showers falling outside the central area. Due to the abundance of large boulders along the array's edge, no MDs have been able to be set up there [1].

electronics and subsequently converted to the total number of particles must be known to better than 5% accuracy in order to achieve a gamma-ray energy resolution of 20% above 100 TeV and 10% above 1 PeV [7].

The traditional calibration procedure usually requires a single-particle spectrum to be measured by setting up the so-called muon telescope systems, as used by GRAPES-3 [8] and ARGO-YBJ experiments [9], or a dedicated trigger logic and data set for single-particle events, used by KASCADE-Grande [10,11] and the Pierre Auger Observatory [12]. It has been demonstrated that on-site measurements of background single particles are effective ways to calibrate the resistive plate chambers, water Cherenkov detectors, and scintillation detectors utilized in earlier investigations. However, this becomes unfeasible for calibrating thousands of detectors over a square kilometer at high altitude, such as for LHAASO, considering the cost of calibration devices and the length of time required for data collecting by the numerous detectors.

Instead, a self-calibration technique that relies on the measurement of single particles within an extensive air shower (EAS) has recently been proposed [13]. This method selects single-particle signals with a high purity from the extremely low-particle-density area far from the shower core. Using a prototype array $\sim 1\%$ the size of

KM2A [14], we have found that this method can determine the output charge of single-particle events with an accuracy of 6% [13]. Nevertheless, the particle density and the resulting single-particle purity derived from the shower simulation depended on the cosmic-ray elemental composition and hadronic interaction model used, thus involving a non-negligible uncertainty. Some improvement should be made to ensure that this method is accurate enough for the KM2A calibration.

In the present work we describe an analysis technique to distinguish characteristic single-particle signals from the EAS data. This method only relies on the statistical description of the shower particles arriving at the detector unit, and does not require prior knowledge of cosmic-ray elemental composition or the hadronic interaction models used to simulate the shower process. The software-based calibration eliminates the need for dedicated data sets acquired using some extra devices, while allowing for the use of the light pulses produced in the sensitive volume of a detector during its science exposure. In this manner, all of the working conditions of the detectors (e.g., temperature, external fields, light yield and signal amplification) are perfectly matched between the calibration and the science data. This analysis also offers an ideal method to monitor the detector performance throughout an expected lifetime of > 10 years.

A brief description of the ED experimental setup and data processing is given in Sec. II. The main principles of this calibration are introduced in Sec. III. A thorough check of the analysis method using simulation data is described in Sec. IV. The whole process of single-particle calibration during KM2A operation is described in Sec. V. The stability and temperature dependence of calibration parameters are investigated in Sec. VI.

II. ED EXPERIMENTAL SETUP AND DATA PROCESSING

In KM2A, 5249 EDs are deployed to measure the number density and arrival time of EAS particles produced by the primary cosmic ray, from which the primary energy and direction can be reconstructed [15]. The ED unit consists of four plastic scintillation tiles (BC-408, made by Saint-Gobain) measuring $100\text{ cm} \times 25\text{ cm} \times 1\text{ cm}$ each (Fig. 2) [16]. The four scintillation tiles are wrapped with Tyvek and placed beneath 1 mm steel and 5 mm lead shielding entailing a threshold of approximately 10 MeV for vertically incident electrons. A 1.5-inch diameter PMT (XP3960, made by HZC Photonics) is coupled to the end of 48 wavelength-shifting fibers (BCF-92SC, made by Saint-Gobain) embedded in the grooves of the scintillation tiles to detect the scintillation photons produced when particles travel through a scintillation tile [17]. For each PMT, a dedicated voltage divider circuit with two outputs (i.e., anode and the sixth dynode) is employed to meet the large dynamic range requirement [18,19]. The anode channel is used to measure particle density up to 200 particles/m², and the dynode channel is used to measure particle density from ~ 100 particles/m² to 10 000 particles/m². Each ED is fully sensitive to the passage of minimum ionizing particles with a detection efficiency above 95% [20].

A very compact front-end electronics (FEE) unit is deployed just behind the PMT of each ED to decrease

transit time delay in the signal cable. Inside each FEE, an analog-to-digital converter (ADC) is used to integrate the PMT signal, and a time-to-digital converter allows the measurement of arrival time with subnanosecond precision [21,22]. Once the PMT signal reaches a fixed amplitude threshold of 1.9 mV (approximately 0.25 times the equivalent pulse height of a single particle), the arrival time and the integrated charge of this signal are digitized by the FEE. Then the digitized data are transmitted to the data acquisition system (DAQ) via optical fibers within a White Rabbit network, which provides subnanosecond time synchronization among all ED FEE nodes [23,24]. The DAQ system is triggered when more than 20 EDs have signals that exceed the threshold within a time window of 400 ns, resulting in an event rate of approximately 2.7 kHz. Once an EAS event is triggered, the ED signals are recorded over a time segment within $\pm 5\ \mu\text{s}$ from the trigger time.

For each ED, the PMT integrated charge recorded by the 12-bit ADC is given in units of ADC channels with a range of 0–4095. During energy reconstruction, the charge should be converted into an equivalent number of particles to provide a common reference level between individual EDs. This conversion is performed using the most probable value of the single-particle response of each ED, both in detector simulation [25] and experimental data. The main goal of charge calibration is to obtain the single-particle spectrum and determine its most probable value in electronics units.

III. ANALYSIS METHOD FOR SINGLE PARTICLES WITHIN AN EAS

When a high-energy cosmic-ray hadron enters the Earth's atmosphere, it interacts with a nucleus from the air (mainly nitrogen and oxygen) at a typical height of 15 to 35 km and produces a shower of secondary particles [26]. The particle densities recorded by the majority of the array detectors are subjected to large fluctuations. Based on

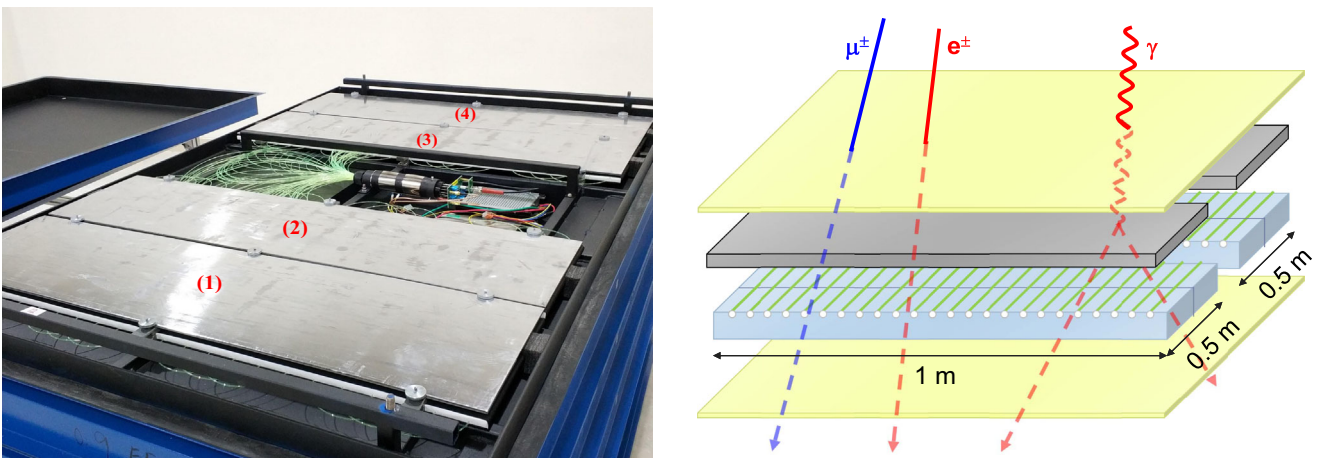


FIG. 2. Left: internal structure of an ED, where the labels (1)–(4) indicate the position of the four scintillation tiles beneath the lead plates. Right: schematic of an ED illustrating how the scintillation tiles are coupled with wavelength-shifting fibers.

experimental data observed at 110 m above sea level, the KASCADE-Grande experiment found that the number of particles recorded by a detector unit obeys Poissonian statistics when the recorded particle number is less than 10. In the case of large particle density, the fluctuations in their measurements seems larger than that calculated when assuming a Poisson process model [10,27]. The quantitative analysis based on the data observed at high altitudes is rarely reported. Nevertheless, it is generally accepted that the Poisson distribution is a reasonable approximation of the particle number detected, especially for sufficiently low particle density, as pointed out in Ref. [28].

We assume that the number of shower particles measured by one ED at a certain location follows a Poisson distribution,

$$P(\mu, n) = \frac{\mu^n e^{-\mu}}{n!}, \quad (1)$$

where μ is the mean number of particles detected by this ED, which depends on the energy of the primary cosmic ray and the distance of the ED to the shower core. Then one can simplify Eq. (1) to the more convenient form

$$\begin{aligned} \mu &= -\ln[P(\mu, 0)] \quad \text{with} \\ P(\mu, 0) &= \frac{N_{\text{null}}}{N} \quad (N_{\text{null}} \neq 0), \end{aligned} \quad (2)$$

where $P(\mu, 0)$ stands for the probability that an ED registers no counts, i.e., is untriggered within a shower event, N is the total number of shower events observed by KM2A over the exposure time and N_{null} is the number of events for which no particles were detected by this ED.

Because the untriggered probability is a function of the distance from the shower core, one can determine the particle density μ at different distances from the core using Eq. (2). Then the probability that a triggered ED registered a single particle can be defined as

$$R = \frac{P(\mu, 1)}{\sum_{n=1}^{\infty} P(\mu, n)} = \frac{\mu}{e^{\mu} - 1}. \quad (3)$$

Defining p as the untriggered probability of the ED at a given core distance, the variance of N_{null} derived from the binomial distribution is $\sigma_{N_{\text{null}}}^2 = Np(1-p)$. Propagating this result into Eq. (2), the statistical uncertainty of μ can be obtained as [29]

$$\sigma_{\mu} = \frac{\sigma_{N_{\text{null}}}}{N_{\text{null}}} = \sqrt{\frac{1}{N_{\text{null}}} - \frac{1}{N}}. \quad (4)$$

Then propagating this result into Eq. (3), the uncertainty of the single-particle purity acquired by this ED is

$$\sigma_R = \frac{1 + \mu e^{\mu} - e^{\mu}}{(e^{\mu} - 1)^2} \cdot \sigma_{\mu}, \quad (5)$$

where σ_{μ} has been obtained by using Eq. (4). The systematic uncertainties will be discussed in the next section.

IV. FEASIBILITY OF THE ANALYSIS METHOD

A. Air shower simulation

The combination of Eqs. (2) and (3) provides an estimator of the particle density and probability of single-particle detection by each ED within an EAS. This estimation, however, is based on the assumption of *a priori* knowledge of the statistical distribution of the shower particles arriving at the detector unit. The real particle density distribution at a fixed core distance based on the EAS simulation needs to be investigated in order to validate this assumption.

Air shower simulations are performed with the program CORSIKA (version 76400) [30]. The hadronic interactions with energies below 80 GeV are treated with the GHEISHA model, and those at higher energy are treated with the QGSJET-II model embedded [31,32]. The electromagnetic interactions are treated with the EGS4 package [33]. About 5.7×10^5 proton-initiated showers are simulated in the primary energy range from 10 to 100 TeV distributed as a power law with a spectral index of -2 . The positions of shower cores are fixed at the point (0, 0). The zenith angles are distributed as $\sin \theta \cdot \cos \theta$ within the zenith angular range $0^\circ < \theta < 45^\circ$, and azimuthal angles are distributed uniformly. The output of this program is a list of all shower particles (above a preset energy threshold of 10 MeV) arriving at the ground together with their coordinates, arrival time, momentum and particle type.

In order to calculate the particle density at different locations, the observation ground is divided into 600×600 bins of 1 m^2 each, equal to the sensitive area of an ED. The actual number of shower particles arriving at these predefined bins around the shower core is averaged over all of the simulated showers and denoted as μ_{ACT} . Meanwhile, the untriggered probability of these bins is derived by counting the number of showers for which no particle arrived at this bin. Using Eq. (2), the particle density is estimated and denoted as μ_{EST} . Figure 3 compares the actual particle density and the estimated value (for gamma rays, electrons, muons, and total particles) in several specific bins, from which a nonignorable bias is observed at distances less than 100 m, particularly for gamma rays and electrons.

We find that the bias arises because the fluctuation of the number of shower particles arriving at 1 m^2 is larger than the expectation of a Poisson distribution, as shown in Fig. 4. This mismatch is probably due to the fact that the gamma rays and electrons within the hadronic shower, especially near the shower core, are not independent. Nevertheless, the estimated particle density agrees well with the actual one for a particle density less than 0.1 m^{-2} , indicating that the Poisson distribution is a good approximation to the number

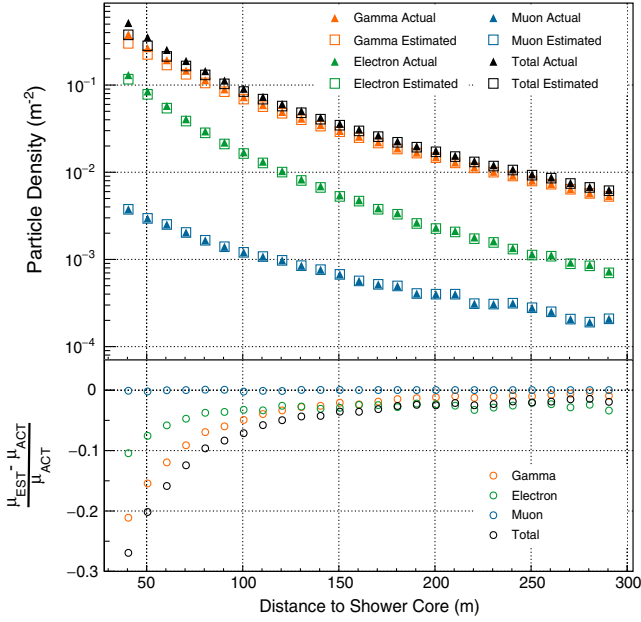


FIG. 3. Top: comparison of the actual simulated particle densities and those estimated from the untriggered fraction, at different distances from the shower core per EAS initiated by protons of 10^{13} – 10^{14} eV (the energies of the simulated events are distributed as a power law with a spectral index of -2). The threshold for shower particles is 10 MeV. Bottom: relative deviation of the estimated particle density from the actual one at different distances from the shower core.

of shower particles arriving at a large distance from the shower core.

B. Systematic effects on the particle density estimation

1. Effects of non-Poissonian fluctuations of shower particles

One can see that only in the case of relatively high particle density, very close to the shower core, do the effects of non-Poissonian fluctuations of shower particles have to be considered for particle density estimation. This problem can be circumvented either by adequate data selection or by applying a bias correction.

In order to avoid a biased measurement of the particle density, the estimated particle density large than 0.1 m^{-2} (thus equivalent to the core distances within 100 m in the primary energy interval between 10 and 100 TeV) arriving at the immediate core region will not be used for the analysis below. With this rigorous standard, the underestimation of the particle density can be limited to less than $6.5 \times 10^{-3} \text{ m}^{-2}$, and consequently the overestimation of the single-particle purity is less than 0.31%, which can be derived from Eq. (5). The systematic errors in the particle density and the single-particle purity are shown in Table I.

2. Variation of the characteristic distance (Molière radius) of the lateral distribution

Multiple Coulomb scattering of electrons (and consequently of the photons) leads to the lateral spread of the shower particles [34]. The length scale of the lateral distribution of shower particles, which can be represented by the Molière radius, varies with altitude, temperature and atmospheric pressure. This variation may lead to biasing in the estimated particle density at a certain core distance.

As discussed in Refs. [28,35], the dependence of the Molière radius (denoted as r_m) on atmospheric conditions can be described as

$$r_m = \frac{73.5}{P - 0.07} \left(\frac{T}{273} \right) \text{ [m]}, \quad (6)$$

where P [atm] and T [K] are the atmospheric pressure and temperature at the observation level. The variations in the observed temperature, atmospheric pressure and calculated Molière radius over one month are shown in Fig. 5, from which the standard deviation of the Molière radius (denoted as Δ_{r_m}) is derived.

Finally, the uncertainty introduced in the particle density amounts to

$$\Delta_{\mu} = \left| \frac{\partial \mu}{\partial r_m} \right| \cdot \Delta_{r_m} \quad \text{with} \quad \mu = \frac{N_e}{2\pi r_m^2} \left(\frac{r}{r_m} \right)^{s-2} \left(1 + \frac{r}{r_m} \right)^{s-4.5} \left(\frac{\Gamma(4.5-s)}{\Gamma(s)\Gamma(4.5-2s)} \right), \quad (7)$$

where μ corresponds to the lateral distribution of the particle density. The expression is known as the Nishimura-Kamata-Greisen function [36,37]. In this function, the variable r represents the distance from the shower axis, and N_e and s denote the shower size and age parameter which can be derived from the shower simulation. One can easily derive the analytical solution of Eq. (7). As a result, the uncertainty of the Molière radius ($\Delta_{r_m} = 2.6 \text{ m}$) on the particle density is $4.3 \times 10^{-4} \text{ m}^{-2}$ at a core distance of 100 m, and $1.4 \times 10^{-4} \text{ m}^{-2}$ at a core distance of 200 m. Using Eq. (5), the uncertainty of the single-particle purity calculated at a core distance of 100 m is 0.021%. We also calculated the uncertainty in the core distance interval between 100 and 300 m; however the result is even smaller (see Table I).

3. Effects related to inclination angles

A variation of the zenith angle results in a change of the atmospheric column density along the shower trajectory between the fringes of the atmosphere and an observer's location, and hence in a change of the development stage of air showers. This implies that the particle density of showers of a given primary energy decrease with increasing

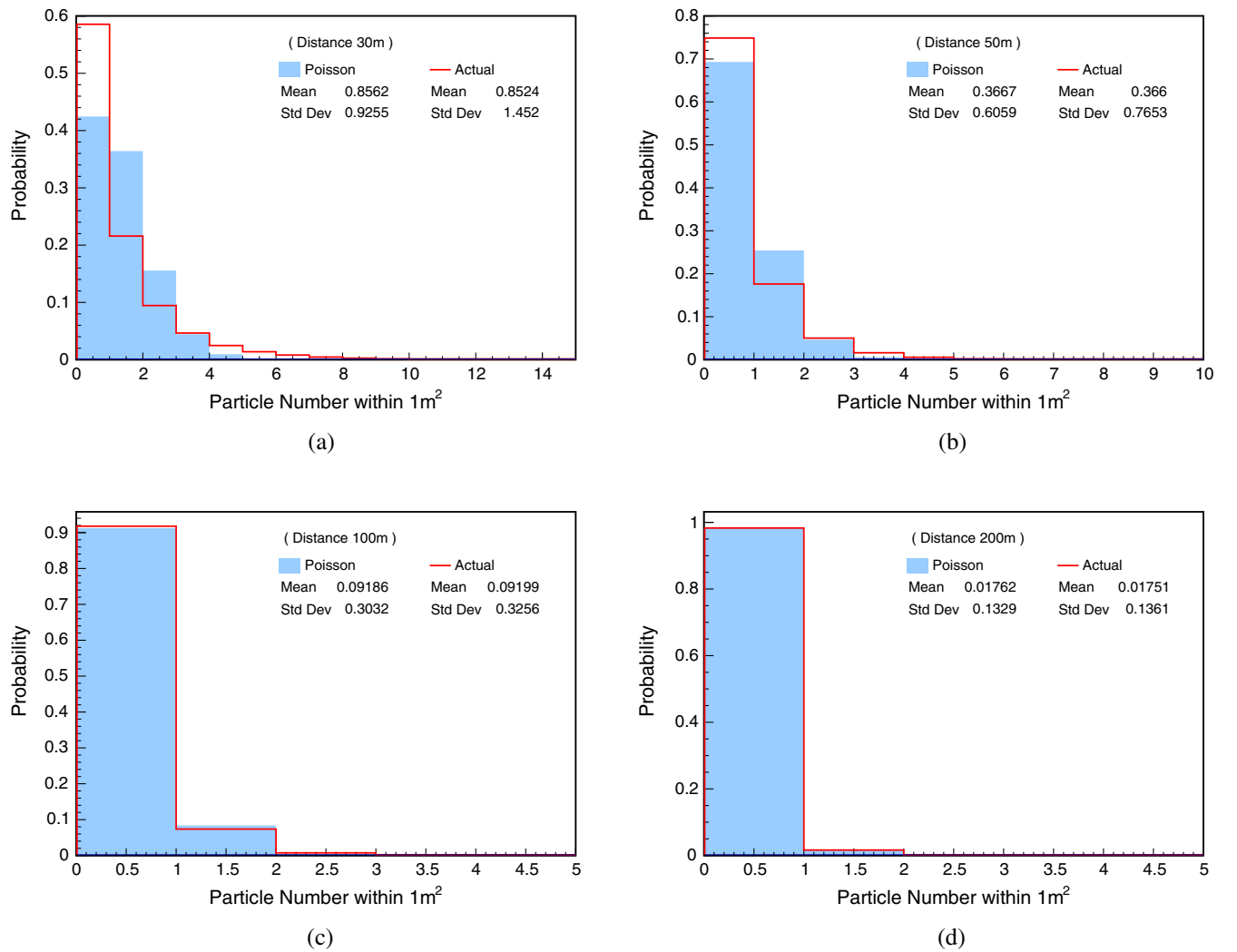


FIG. 4. Probability distribution of the number of shower particles arriving at a given 1 m² area, located at a distance from the shower core of (a) 30 m, (b) 50 m, (c) 100 m, and (d) 200 m. A Poisson distribution with the same mean value is also illustrated for comparison. The small difference in their mean values is caused by the cutoff value of the horizontal axis.

zenith angle (if observed below the shower maximum) and the average path length of the particles in the detectors increases.

Specific simulations for different zenith angle intervals ($0^\circ < \theta < 15^\circ$, $15^\circ < \theta < 30^\circ$, $30^\circ < \theta < 45^\circ$) are performed to identify any effects on the particle density estimation due to the inclination angles. Figure 6 compares

the actual particle density and the estimated value for three zenith angle intervals. The particle density arriving at the observation level manifests a zenith angle dependence, while only a negligible dependence of the relative error on zenith angle is observed. The systematic impact of non-Poissonian fluctuations on particle density estimation is still present even at the large zenith angles. To ensure

TABLE I. Summary of systematic uncertainties derived from air shower simulations. Instrumental effects and other effects related to shower reconstruction are discussed in Sec. V.

Item	Core distance of 50 m		Core distance of 100 m		Core distance of 200 m	
	$\Delta_\mu(\text{m}^{-2})$	Δ_R	$\Delta_\mu(\text{m}^{-2})$	Δ_R	$\Delta_\mu(\text{m}^{-2})$	Δ_R
Non-Poissonian fluctuation of particle density	7.1×10^{-2}	3.1%	6.5×10^{-3}	0.31%	4.4×10^{-4}	0.022%
Variation of r_m due to atmospheric conditions	4.6×10^{-5}	0.002%	4.3×10^{-4}	0.021%	1.4×10^{-4}	0.007%
Total	7.1×10^{-2}	3.1%	6.5×10^{-3}	0.31%	4.6×10^{-4}	0.023%

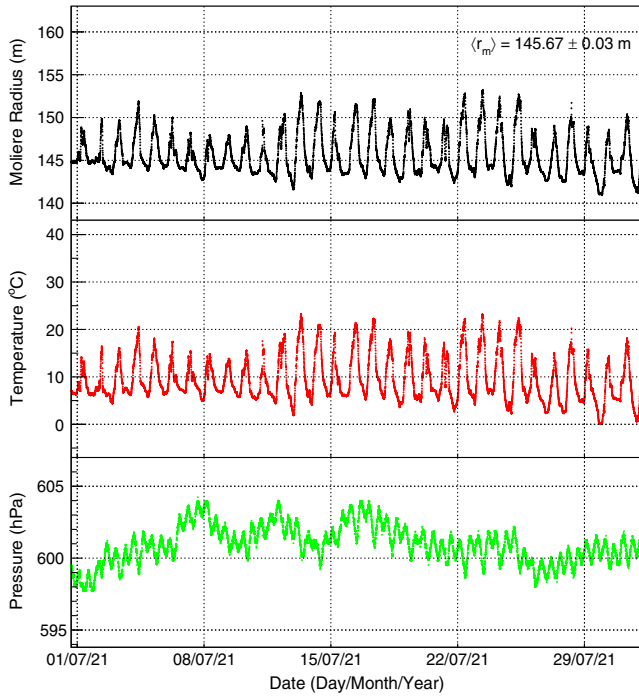


FIG. 5. Variation in the calculated Molière radius (top), the observed temperature (middle) and atmospheric pressure (bottom) for a period of 31 days in July 2011.

sufficient statistics in the overall calibration, the showers with zenith angles less than 45° are used for the analysis below.

4. Effects related to hadronic interaction models

The present method only depends on the statistical description of the shower particles arriving at the observation level; however, the feasibility of this method have to be validated by simulating these air showers. In this perspective, the reliability of air shower simulations is important for estimating particle densities.

A specific comparison of different hadronic interaction models (QGSJET-II and EPOS) in the simulation is performed to assess any effects related to interaction models. In principle all of the hadronic interaction models used in the air shower simulations are based on similar concepts (e.g., unitarity and analyticity of the scattering amplitude, minijet production, string fragmentation) but differ in the degree of detail in the implementation of these concepts [26]. QGSJET-II is based on the Gribov-Regge theory of multi-Pomeron exchange to model high-energy hadronic interactions. It and its previous version QGSJET-I have been widely used in cosmic-ray physics for many years. EPOS is based on a microscopic Pomeron model in which the Pomeron-parton coupling, including momentum sharing, is explicitly calculated [38,39].

Figure 7 compares the actual particle density (including gamma rays, electrons and muons) and the estimated values

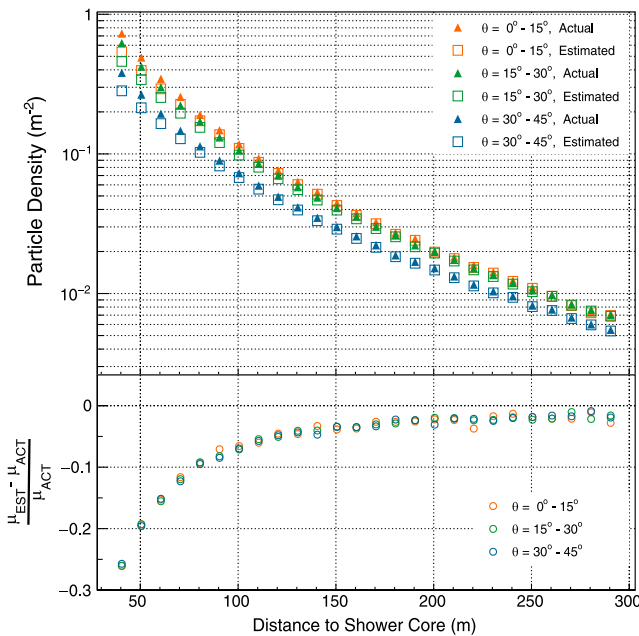


FIG. 6. Top: comparison of the actual simulated particle densities and those estimated from the untriggered fraction for different zenith angle intervals. Bottom: relative deviation of the estimated particle density from the actual one at different distances from the shower core.

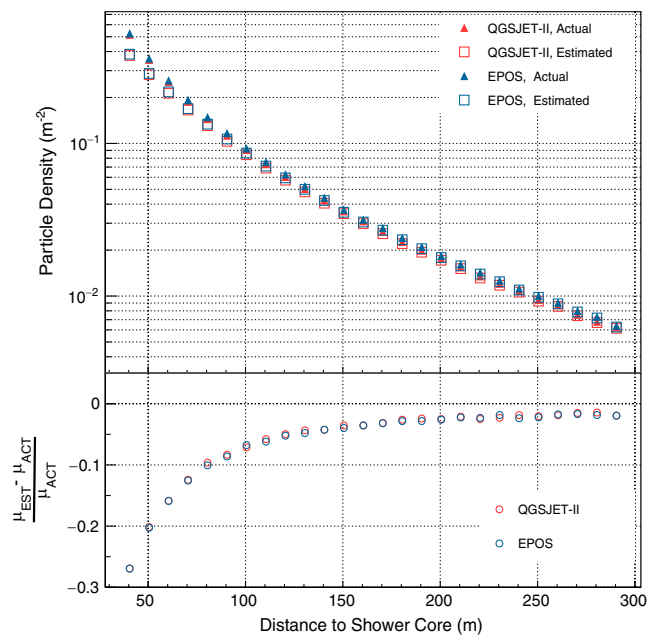


FIG. 7. Top: comparison of the actual simulated particle densities and those estimated from the untriggered fraction for different hadronic interaction models used in shower simulations. Bottom: relative deviation of the estimated particle density from the actual one at different distances from the shower core.

for different interaction models. The particle density simulated by the EPOS model is overall 2% higher than the one simulated by the QGSJET-II model. It is clear that the analysis approach is independent of the model in this energy interval because there is no noticeable difference between the relative errors of estimated particle density produced from the two subsamples.

All of the systematic uncertainties derived from the air shower simulations are shown in Table I. Other effects related to detector performances (e.g., detector noise, nonlinear responses) and reconstruction of the shower cores will be discussed in Sec. V.

V. CHARGE CALIBRATION USING KM2A DATA

During KM2A operation, there are four steps for the charge calibration.

- (1) Determination of the most probable value (MPV) of the EAS particle spectrum for each ED. This provides an initial coefficient of the conversion from ADC channels to number of particles, which is necessary to reconstruct the shower core and direction for the following steps.
- (2) Determination of the ED untriggered probability at different distances from the shower core.
- (3) Calibration of the MPV of the single-particle spectrum selected from EAS data.
- (4) Calibration of the gain ratio between the anode and the sixth dynode (DY6) in their overlap ranges, in order to transfer the calibration parameter of the anode channel to the DY6 channel in case the former is saturated.

A. Determination of the MPV of the EAS particle spectrum

Arising from the fact that the number of shower particles (irrespective of shower size and location of the shower core) detected by each detector during data taking follows an exponential distribution with a slope close to the energy spectrum index of the primary cosmic rays [28,37,40], the MPV of the shower particle spectrum is dominated by single-particle events, thus providing an estimation of the output charge corresponding to a single particle.

The shower particle spectrum is obtained from the ED signals within a time window of ± 150 ns from the trigger time. As an example, the particle spectrum of one ED (anode channel) during 4 hours of stable operation is shown in Fig. 8. The first peak around 10 ADC channels is caused by the convolution of the trigger with the falling distribution of low-energy particles. The second peak around 20 ADC channels is dominated by energetic single particles within showers. Fitting this distribution with a Gaussian yields a peak value of 22.62 ± 0.11 ADC channels/particle. The coefficient of each ED is utilized to convert the

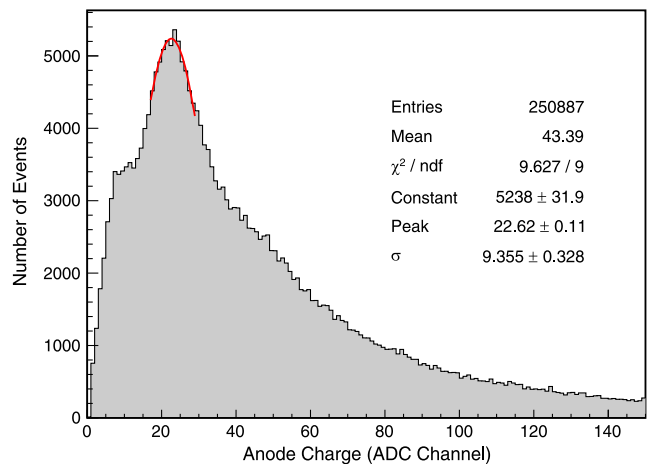


FIG. 8. An example of an EAS particle spectrum in ADC channel units for one ED (ID 2325). A Gaussian function is fitted to the peak of the distribution.

integrated charge to the number of particles for the subsequent shower reconstruction [7].

It should be mentioned that the high voltage of each PMT has been adjusted to obtain the MPV of the charge distribution around 20 ADC channels, to ensure that the anode signal can cover the dynamic range of 1–200 particles.

B. Determination of the ED untriggered probability

After the shower core and direction reconstruction, the ED untriggered probability is measured using a set of EAS events through the following sequence.

First, we search a set of showers with a total number of triggered EDs less than 80 (to guarantee shower energies of less than 100 TeV) and shower cores located at a distance from 100 to 101 m (i.e., in a loop with 1 m width, as shown in Fig. 9) around a certain ED, and count the number of these showers (denoted as N). Meanwhile, we count the number of showers for which there were no particles detected by this ED (denoted as N_{null}) within $(-50, 100)$ ns around the shower front. Then the untriggered probability and particle density at this radius from the shower core are calculated using Eq. (2). Repeating this process by increasing the core distance from this ED in 10-m steps, the particle density with respect to the distance from shower core is obtained, as shown in Fig. 10. The corresponding single-particle purity at different radii is estimated using Eq. (3) and also illustrated in Fig. 10, from which one can infer that the probability of detecting only a single particle is greater than 98% when the core distance is larger than 100 m. Note that the difference in the estimated particle density between Figs. 3 and 10 occurs because the simulated data uses the arriving particle density and the experimental data uses the detecting particle density [the trigger efficiency of individual ED for gamma-rays (> 10 MeV) is about 40%].

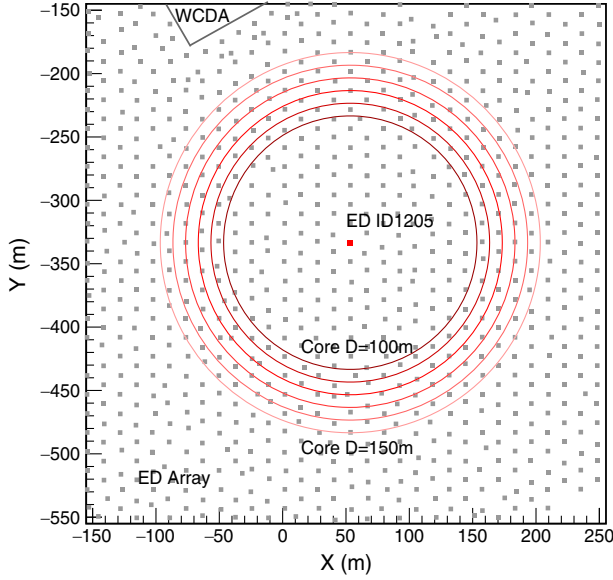


FIG. 9. Schematic of different distances from one ED (ID 1205) at which shower cores are analyzed. The boxes represent EDs and the colored circles indicate the analyzed shower core locations from 100 to 150 m. The box sizes and line widths are exaggerated for better visibility.

Typically, spurious signals due to the background (e.g., the random signals of environmental radioactivity) above the threshold can lead to overestimating the particle density (and consequently underestimating the single-particle purity). Hence the assertion of the null signal counts N_{null} in Eq. (2) must be cleaned from the background above the threshold, detector by detector, as

$$N_{\text{null}} = N - N_{\text{fire}} + N_{\text{bg}}, \quad (8)$$

where N_{fire} is the number of all signals (including EAS particles and background) above the threshold during the

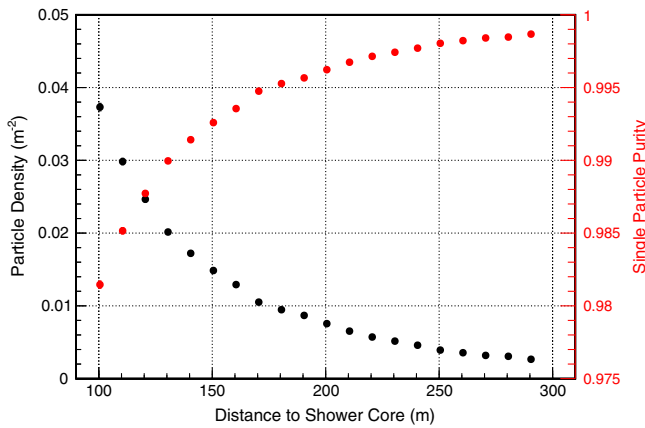


FIG. 10. Estimated particle density at different distances from the shower core. The corresponding single-particle purity is also illustrated in this figure.

exposure time, and N_{bg} is the number of background signals above the threshold during exposure.

The background events are dominated by the environmental radioactivity, individual minimum ionizing particles and detector noise, which are specific to a given experiment because they depend on the altitude of observation site as well as the detector thresholds. The number of background signals above the detector threshold during the exposure time can be derived from a Poisson distribution as

$$N_{\text{bg}} = N(1 - e^{-rT}) \simeq NrT \quad \text{for } (rT \ll 1), \quad (9)$$

where r is the counting rate of background signals, T is the exposure time window of signal collection for each shower, and rT represents the number of background signals recorded by an ED within the time window. Typically, the background particles pass through an ED with a counting rate of approximately 1.5 kHz, with a nonuniformity of 10%. Additionally, time constraints have been applied. In order to achieve a high signal-to-noise ratio, the time window T is set to $(-50, 100)$ ns around the shower front, so the background event counts N_{bg} are only 0.023% of the total shower counts N . If the spurious signals are not eliminated, the error in the single-particle purity introduced by spurious signals is less than 0.02%.

C. Calibration of the MPV of the single-particle spectrum

The single particles within an EAS as recorded by each ED are selected for calibration if they fulfill certain conditions, which can be summarized as follows:

- (1) The zenith angle of the shower is less than 45° , to ensure that the event is well reconstructed.
- (2) The shower core is located within the area of the array, to ensure a reliable reconstruction of the shower core.
- (3) For each shower, the total number of triggered EDs is less than 80, corresponding to a primary energy below ~ 100 TeV.
- (4) The radial distance ranges from 100 to 300 m between the shower core and the associated ED under calibration.
- (5) The arrival time of particles is within $(-50, 100)$ ns around the shower front, to suppress background or detector noise during exposure.

The resulting single-particle spectrum of one ED (anode channel) during 4 hours of data taking is shown in Fig. 11. Considering the large energy depositions produced by electron-positron pairs when a single gamma ray travels through the lead, the distribution is different from the single-muon spectrum measured at low altitude [20]. Because a Landau function cannot fit the data well, the MPV of the single-particle spectrum is obtained by means of Gaussian fits to the ± 6 ADC channels around the peak.

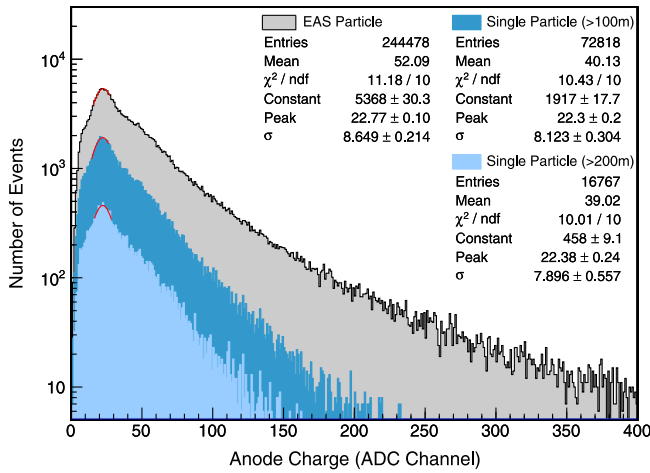


FIG. 11. Single-particle spectrum of one ED (ID 1205) acquired from the EAS data (cyan histogram for core distance larger than 100 m, and azure histogram for core distance larger than 200 m). The EAS particle spectrum (gray histogram) is also illustrated for comparison.

The single-particle spectrum (cyan histogram in Fig. 11) displays a decreasing at large anode charges when compared to the shower particle spectrum (gray histogram in Fig. 11), and as a result, a 23% decrease in average output charge is seen. These characteristics can be understood as the suppression of multiparticle contamination, the value of which depends on the single-particle purity after data selection. Although applying the stricter cut with larger distance or lower primary energy can improve the purity of single-particle events (e.g., azure histogram in Fig. 11), this requires more exposure time to collect enough events, thus slowing down the calibration.

During KM2A operation, the single-particle calibration is carried out once every 4 hours, resulting in a statistical error less than 1%. It is possible to use the experimental data directly to study the accuracy of the MPV derived from the single-particle spectrum. For this purpose we compare the MPVs with the ones derived from the higher-purity single-particle spectrum for core distances between 200 and 300 m, detector by detector (an example is shown in Fig. 11). This yields a residual error of 0.4%. However, this approach cannot measure the systematic errors shared by both event subsamples. For example, the bias due to the intrinsic features of showers (as mentioned in Sec. IV) would be free from this error. All of the systematic uncertainties will be discussed in Sec. VE.

D. Calibration of the gain ratio between the anode and DY6

As mentioned in Sec. II, two output channels of each ED-PMT are read out to meet the requirement of large dynamic range. Once a large number of particles pass through an ED, the anode channel is saturated and the signal from the DY6 is employed instead. Because the gain

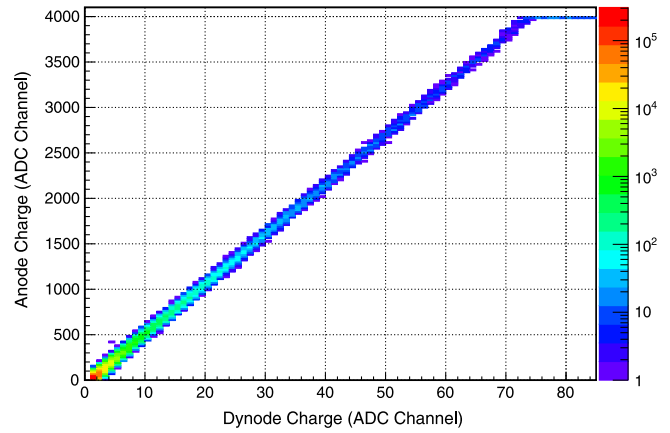


FIG. 12. Correlation between the anode and DY6 output charge for one ED (ID 998), acquired from the EAS data. The color spectrum represents the number of events in each bin.

of the amplified DY6 is approximately one-fiftieth of the anode gain, the single-particle signal is too low to be distinguished from the DY6 channel. Therefore, the DY6 and anode are cross calibrated in their overlap ranges (~ 100 – 200 particles/m²) using EAS data.

From the EAS data acquired over one day of continuous stable operation, a significant correlation between the anode and DY6 output charge is observed (Fig. 12). The gain ratio between the anode and DY6 is calculated event by event and plotted as a function of the anode output charge, as shown in Fig. 13. The flat region from ~ 1500 to 4000 ADC channels corresponds to the overlap range, over which both the anode and DY6 response to the incident particle density are linear. In the lower particle density region, the precision of the DY6 channel decreases and a deviation occurs. The determination of the gain ratio requires a suitable cut of the anode charge to avoid a biased measurement. The gain ratio is finally determined

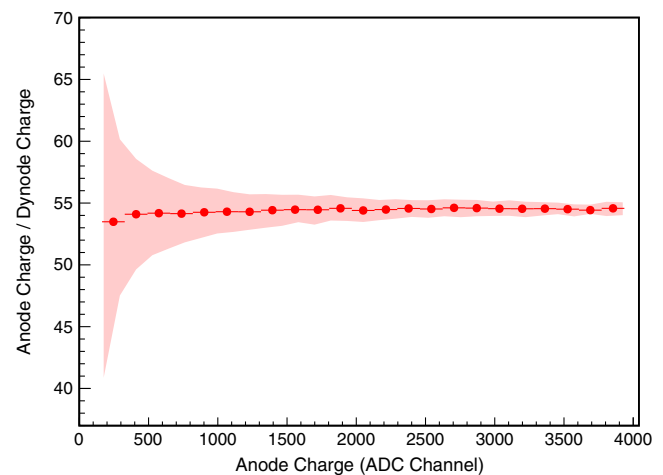


FIG. 13. Gain ratio between the anode and DY6 versus the anode output charge for one ED (ID 998). The red zone depicts the data's dispersion (standard deviation) for each bin.

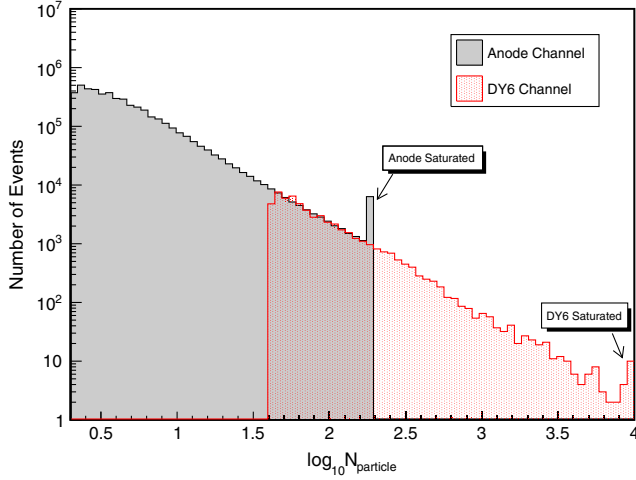


FIG. 14. EAS particle spectrum for one ED (ID 998). The horizontal axis shows the equivalent number of minimum ionizing particles on a log scale.

by averaging the ratio value in the overlap range, with a statistical error of 0.2%. Then the gain ratio is utilized to transfer the calibration parameter of the anode channel to the DY6 channel. The anode signal fluctuations that cause bin-to-bin migrations are the source of the systematic error. This yields a slight bias within 0.2%, which depends on the fluctuation amplitude of anode signals and the slope in the low-anode-charge region.

After transferring the single-particle calibration of the anode channel to the DY6 channel, the particle spectrum of each ED is finally obtained. Figure 14 shows as an example the particle spectrum recorded by one ED. The anode channel ADC tends to saturate at a particle density of 200 particles/m², and the DY6 remains linear up to 10000 particles/m². The combination of these two channels allows an overall dynamic range of 10⁴.

E. Achievable accuracy

The calibration is affected by several systematic uncertainties, which are summarized in Table II.

For the single-particle calibration (anode channel), the first three items have been discussed above. The non-linearity responses of the anode charge around 20 ADC channels introduces an uncertainty of less than 1.0%. This effect has been carefully treated in the hardware design of the PMTs and FEE and tested in the laboratory [17]. Besides, the anode gain slightly changes with ambient temperature, leading to an uncertainty of less than 1.2% when assuming a reasonable temperature variation of 7 °C during 4 hours of data taking. The temperature effect has been observed and studied from the ED monitoring data. As a result, the total uncertainty of the anode channel is less than 2.0% after adding each contribution quadratically.

For the cross calibration (DY6 channel), the uncertainty is dominated by the uncertainty of the anode calibration. Other effects contribute a negligible uncertainty.

VI. STABILITY OF CALIBRATION PARAMETERS

The software-based calibration provides a robust method for monitoring detector performance during its science exposure. The stability of the single-particle spectrum is an important parameter to monitor the single-particle response and its degradation through their lifetime.

Figure 15 shows the distribution of calibration parameters for all EDs under operation on October 1, 2021. Some EDs have parameters that are higher (or lower) than those of the majority of EDs because a higher (or lower) level of PMT voltage was used. Figure 16 shows the variation of the calibration parameters and the interior temperature of one ED from September 2021 to December 2021. The single-particle response shows an inverse dependence on the temperature. This effect can be understood as an overall

TABLE II. Summary of systematic uncertainties of charge calibration for EDs.

Item	Uncertainty	Comments
Anode channel (single-particle calibration)		
Systematic uncertainties derived from shower simulation	< 0.31%	Requires a suitable particle density cut (< 0.1 m ⁻²) or core distance (> 100 m), as outlined in Table I
Multiparticle contamination	< 0.4%	Residual error mentioned in Sec. V C
Spurious signals from background	...	Requires an unbiased correction; otherwise, < 0.02%
Nonlinear response	< 1.0%	Requires previous laboratory testing
Temperature effect of anode gain	< 1.2%	Through regular calibration, which is carried out once every 4 hours
Statistical error of fitting	< 1.0%	
Total	< 2.0%	
DY6 channel (cross calibration)		
Calibration for anode channel	< 2.0%	All of the errors mentioned above
Bin-to-bin migrations due to fluctuation	< 0.2%	Requires a suitable cut of anode charge; can also be corrected using unfolding methods
Temperature effect of gain ratio	< 0.2%	Through regular calibration, which is carried out once every 4 hours
Statistical error of gain ratio	< 0.2%	
Total	< 2.0%	

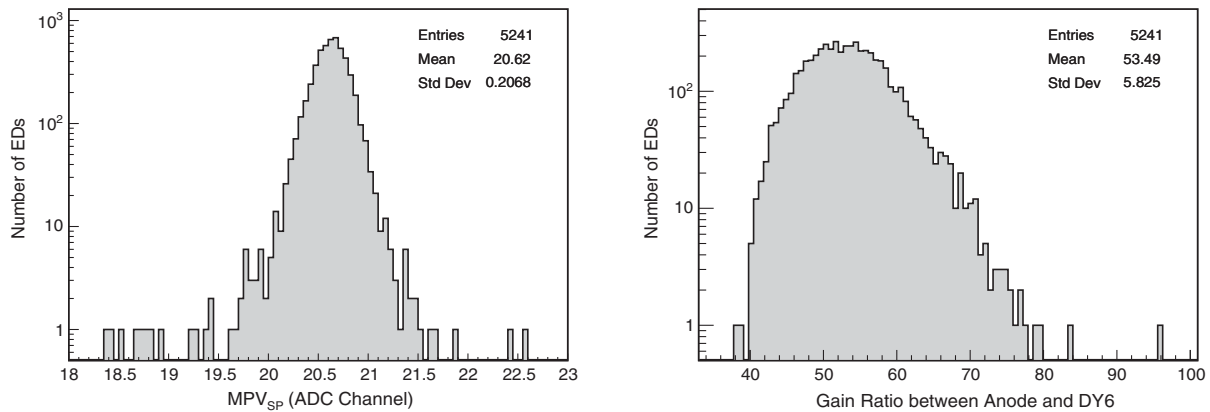


FIG. 15. Distribution of calibration parameters including the MPV of the single-particle spectrum (left) and the gain ratio of the anode to DY6 (right), for all EDs under operation on October 1, 2021.

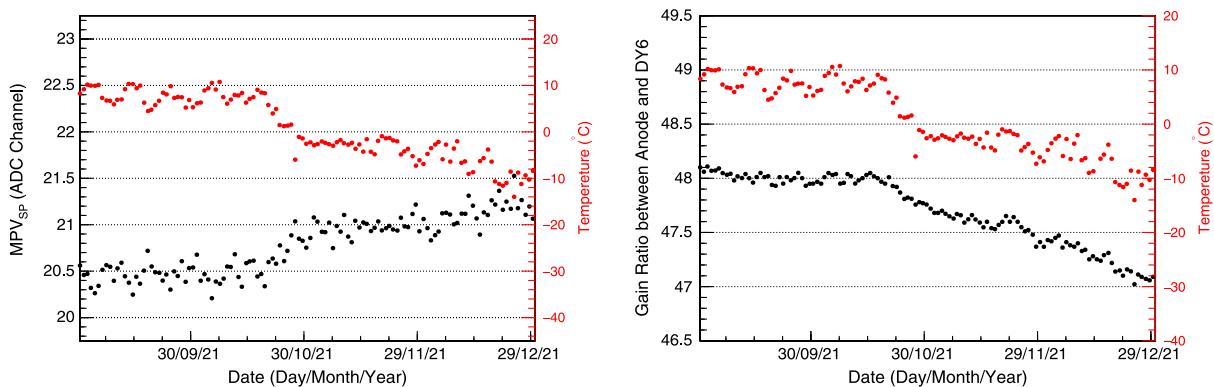


FIG. 16. Left: time variation of the MPV of the single-particle spectrum (black points) and the temperature (red points) for one ED (ID 1361) from September 2021 to December 2021. Each point is averaged over the calibration parameters for each day, and thus the diurnal variations are not visible. Right: variation of the gain ratio (black points) and the temperature (red points) for one ED (ID 1361) from September 2021 to December 2021.

temperature dependence of the scintillator tiles, fibers, PMT and FEE. According to the laboratory characterization, the PMT gain has a temperature coefficient of $-0.09\%/^{\circ}\text{C}$ [17]. A more detailed study is underway to evaluate whether the fibers contribute the remaining part of this variation. During KM2A operation, the single-particle calibration is carried out once every 4 hours, and thus the diurnal variation can be easily calibrated.

VII. SUMMARY AND CONCLUSIONS

A reliable and automatic calibration technique is necessary for next-generation gamma-ray observatories like LHAASO. The analysis of single particles within EAS has been shown to be a powerful method to calibrate thousands of EDs in its square kilometer array. In order to reduce the uncertainty due to the imperfect knowledge of the cosmic-ray elemental composition and hadronic interaction model, the detector untriggered probability was proposed to estimate the particle density and single-particle purity at different distances from the shower core.

Even though such an analysis has a systematic bias near the shower core, it provides a reliable estimation of the particle density at a large core distance. Experimental results have shown that the single-particle calibration can be used to determine the equivalent particle number with an accuracy better than 2.0% within a time scale of hours. This accuracy is adequate for energy reconstruction.

Besides this, the number of muons within showers detected at a certain location follows a Poisson distribution (as shown in Fig. 3). Muons are the decay products of hadrons and undergo less atmospheric interactions than electromagnetic particles, making them ideal “probes” to understand the hadronic interaction processes [14]. In this sense, the proposed method offers a separate measurement of the muonic component within EAS using muon detectors, which plays a crucial role in studying hadronic interaction models and cosmic-ray mass compositions at the high energies of interest [41,42].

In principle, this method can be also applied to other EAS experiments which comprise a huge number of detectors.

ACKNOWLEDGMENTS

We thank all staff members who work at the LHAASO site to maintain the detector and keep the electricity power supply and other components of the experiment operating smoothly. We are particularly grateful to H. H. He and S. Z.

Chen for their assistance in this study and encouragement. This work is supported in China by the National Key R&D program of China under Grant 2018YFA0404201, and by the National Natural Science Foundation of China (Grant No. 12105301).

-
- [1] Z. Cao, F. A. Aharonian *et al.* (LHAASO Collaboration), Ultrahigh-energy photons up to 1.4 petaelectronvolts from 12γ -ray Galactic sources, *Nature (London)* **594**, 33 (2021).
- [2] Z. Cao, F. Aharonian *et al.* (LHAASO Collaboration), PeV gamma-ray emission from the Crab Nebula, *Science* **373**, 425 (2021).
- [3] F. Aharonian, Q. An *et al.* (LHAASO Collaboration), Extended Very-High-Energy Gamma-Ray Emission Surrounding PSR J0622 + 3749 Observed by LHAASO-KM2A, *Phys. Rev. Lett.* **126**, 241103 (2021).
- [4] Z. Cao, F. Aharonian *et al.* (LHAASO Collaboration), Discovery of a new gamma-ray source, LHAASO J0341+5258, with emission up to 200 TeV, *Astrophys. J. Lett.* **917**, L4 (2021).
- [5] Z. Cao, F. Aharonian *et al.* (LHAASO Collaboration), Discovery of the ultrahigh-energy gamma-ray source LHAASO J2108 + 5157, *Astrophys. J. Lett.* **919**, L22 (2021).
- [6] X. Ma, Y. Bi *et al.*, Chapter 1 LHAASO instruments and detector technology, *Chin. Phys. C* **46**, 030001 (2022).
- [7] F. Aharonian, Q. An *et al.* (LHAASO Collaboration), Observation of the Crab Nebula with LHAASO-KM2A-a performance study, *Chin. Phys. C* **45**, 025002 (2021).
- [8] S. Gupta, Y. Aikawa *et al.* (The GRAPES-3 Collaboration), GRAPES-3-A high-density air shower array for studies on the structure in the cosmic-ray energy spectrum near the knee, *Nucl. Instrum. Methods Phys. Res., Sect. A* **540**, 311 (2005).
- [9] G. Aielli, C. Bacci *et al.*, Calibration of the RPC charge readout in the ARGO-YBJ experiment, *Nucl. Instrum. Methods Phys. Res., Sect. A* **661**, S56 (2012).
- [10] W. Apel, J. Arteaga *et al.*, The KASCADE-Grande experiment, *Nucl. Instrum. Methods Phys. Res., Sect. A* **620**, 202 (2010).
- [11] T. Antoni, W. Apel *et al.* (KASCADE Collaboration), The cosmic-ray experiment KASCADE, *Nucl. Instrum. Methods Phys. Res., Sect. A* **513**, 490 (2003).
- [12] X. Bertou, P. Allison *et al.*, Calibration of the surface array of the Pierre Auger Observatory, *Nucl. Instrum. Methods Phys. Res., Sect. A* **568**, 839 (2006).
- [13] H. Lv, H. He *et al.*, Calibration of the LHAASO-KM2A electromagnetic particle detectors using charged particles within the extensive air showers, *Astropart. Phys.* **100**, 22 (2018).
- [14] C. Li, H. He *et al.* (LHAASO Collaboration), Measurement of muonic and electromagnetic components in cosmic ray air showers using LHAASO-KM2A prototype array, *Phys. Rev. D* **98**, 042001 (2018).
- [15] H. He, Design of the LHAASO detectors, *Radiat. Detect. Technol. Methods* **2**, 7 (2018).
- [16] Y. Wang, C. Hou *et al.*, Testing and analysis of the plastic scintillator units for LHAASO-ED, *Radiat. Detect. Technol. Methods* **5**, 513 (2021).
- [17] Y. Yu, H. Lv, X. Sheng, D. Liu, and C. Feng, Performance test and qualification of the photomultiplier tube for the whole production of LHAASO-ED, *Nucl. Instrum. Methods Phys. Res., Sect. A* **1025**, 166120 (2022).
- [18] Y. Yu, H. Lv, K. Tariq, D. Liu, X. Sheng, and C. Feng, Study of the performance of photomultiplier tubes at high variable counting rates, *Nucl. Instrum. Methods Phys. Res., Sect. A* **1008**, 165433 (2021).
- [19] H. Lv, X. Sheng, H. He, J. Liu, Z. Zhang, C. Hou, and J. Zhao, Extension of photomultiplier tube dynamic range for the LHAASO-KM2A electromagnetic particle detectors, *Nucl. Instrum. Methods Phys. Res., Sect. A* **781**, 34 (2015).
- [20] F. Aharonian, Q. An *et al.* (LHAASO Collaboration), Performance test of the electromagnetic particle detectors for the LHAASO experiment, *Nucl. Instrum. Methods Phys. Res., Sect. A* **1001**, 165193 (2021).
- [21] X. Liu, J. Chang, Z. Wang, and L. Fan, Prototype of readout electronics for the LHAASO KM2A electromagnetic particle detectors, *Chin. Phys. C* **40**, 076101 (2016).
- [22] W. Pan, G. Gong, Q. Du, H. Li, and J. Li, High resolution distributed time-to-digital converter (TDC) in a White Rabbit network, *Nucl. Instrum. Methods Phys. Res., Sect. A* **738**, 13 (2014).
- [23] Q. Du, G. Gong, and W. Pan, A packet-based precise timing and synchronous DAQ network for the LHAASO project, *Nucl. Instrum. Methods Phys. Res., Sect. A* **732**, 488 (2013).
- [24] F. Yang, J. Chang *et al.*, LHAASO KM2A distributed long-distance data transmission, *Radiat. Detect. Technol. Methods* **3**, 43 (2019).
- [25] S. Chen, Detector Simulation of LHAASO-KM2A with Geant4, *Proc. Sci. ICRC2019* (2019) 219.
- [26] R. Engel, D. Heck, and T. Pierog, Extensive air showers and hadronic interactions at high energy, *Annu. Rev. Nucl. Part. Sci.* **61**, 467 (2011).
- [27] W. Apel, A. Badea *et al.*, Comparison of measured and simulated lateral distributions for electrons and muons with KASCADE, *Astropart. Phys.* **24**, 467 (2006).
- [28] P. K. Grieder, *Extensive Air Showers* (Springer, Berlin, Heidelberg, 2010).
- [29] F. Neves, V. Chepel, D. Yu. Akimov, H. M. Araújo, E. J. Barnes, V. A. Belov, A. A. Burenkov, A. Currie, B. Edwards, C. Ghag, M. Horn, A. J. Hughes, G. E. Kalmus,

- A. S. Kobyakin, A. G. Kovalenko, V. N. Lebedenko, A. Lindote, M. I. Lopes, R. Lüscher, K. Lyons, P. Majewski, A. St. J. Murphy, J. Pinto da Cunha, R. Preece, J. J. Quenby, P. R. Scovell, C. Silva, V. N. Solovov, N. J. T. Smith, P. F. Smith, V. N. Stekhanov, T. J. Sumner, C. Thorne, and R. J. Walker, Calibration of photomultiplier arrays, *Astropart. Phys.* **33**, 13 (2010).
- [30] D. Heck, J. Knapp *et al.*, CORSIKA: A Monte Carlo code to simulate extensive air showers, Technical Report No. FZKA-6019, 1998.
- [31] S. Ostapchenko, QGSJET-II: Towards reliable description of very high energy hadronic interactions, *Nucl. Phys. B, Proc. Suppl.* **151**, 143 (2006).
- [32] S. Ostapchenko, Nonlinear screening effects in high energy hadronic interactions, *Phys. Rev. D* **74**, 014026 (2006).
- [33] W. R. Nelson and D. W. O. Rogers, Structure and operation of the egs4 code system, in *Monte Carlo Transport of Electrons and Photons*, edited by T. M. Jenkins, W. R. Nelson, and A. Rindi (Springer, US, Boston, MA, 1988), pp. 287–305.
- [34] G. Molière, Theorie der streuung schneller geladener teilchen ii mehrfach-und vielfachstreuung, *Z. Naturforsch. A* **3**, 78 (1948).
- [35] G. Cocconi, Extensive air showers, in *Cosmic Rays I / Kosmische Strahlung I*, edited by S. Flügge (Springer Berlin Heidelberg, Berlin, Heidelberg, 1961), pp. 215–271.
- [36] K. Kamata and J. Nishimura, The lateral and the angular structure functions of electron showers, *Prog. Theor. Phys. Suppl.* **6**, 93 (1958).
- [37] K. Greisen, Cosmic ray showers, *Annu. Rev. Nucl. Sci.* **10**, 63 (1960).
- [38] K. Werner, F.-M. Liu, and T. Pierog, Parton ladder splitting and the rapidity dependence of transverse momentum spectra in deuteron-gold collisions at the BNL relativistic heavy ion collider, *Phys. Rev. C* **74**, 044902 (2006).
- [39] M. Hladik, H. J. Drescher, S. Ostapchenko, T. Pierog, and K. Werner, Self-Consistency Requirement in High-Energy Nuclear Scattering, *Phys. Rev. Lett.* **86**, 3506 (2001).
- [40] P. Mohanty, S. Dugad *et al.*, Measurement of some EAS properties using new scintillator detectors developed for the GRAPES-3 experiment, *Astropart. Phys.* **31**, 24 (2009).
- [41] G. Wilk and Z. Włodarczyk, On the chemical composition of cosmic rays of highest energy, *J. Phys. G* **38**, 085201 (2011).
- [42] W. Apel, J. Arteaga-Velázquez *et al.*, The kascade-grande energy spectrum of cosmic rays and the role of hadronic interaction models, *Adv. Space Res.* **53**, 1456 (2014).